Correlated Magnetic Weyl Semimetal State in Strained $Pr_2Ir_2O_7$

Yangyang Li,* Taekoo Oh, Jaeseok Son, Jeongkeun Song, Mi Kyung Kim, Dongjun Song, Sukhyun Kim, Seo Hyoung Chang, Changyoung Kim, Bohm-Jung Yang, and Tae Won Noh*

Correlated topological phases (CTPs) with interplay between topology and electronic correlations have attracted tremendous interest in condensed matter physics. Therein, correlated Weyl semimetals (WSMs) are rare in nature and, thus, have so far been less investigated experimentally. In particular, the experimental realization of the interacting WSM state with logarithmic Fermi velocity renormalization has not been achieved yet. Here, experimental evidence of a correlated magnetic WSM state with logarithmic renormalization in strained pyrochlore iridate $Pr_2Ir_2O_7$ (PIO) which is a paramagnetic Luttinger semimetal in bulk, is reported. Benefitting from epitaxial strain, "bulk-absent" all-in–all-out antiferromagnetic ordering can be stabilized in PIO film, which breaks time-reversal symmetry and leads to a magnetic WSM state. With further analysis of the experimental data and renormalization group calculations, an interacting Weyl liquid state with logarithmically renormalized Fermi velocity, similar to that in graphene, is found, dressed by long-range Coulomb interactions. This work highlights the interplay of strain, magnetism, and topology with electronic correlations, and paves the way for strain-engineering of CTPs in pyrochlore iridates.

1. Introduction

Electronic-correlation-driven physics and topological nontrivial physics are two central threads of modern condensed matter research,[1] and have drawn intensive investigations independently. Electronic correlations (U) have been well studied in the last several decades[2–4] and play a crucial role in generating various exotic quantum phenomena, such as metal–insulator transition,[2] colossal magnetoresistance,[3] and unconventional superconductivity.[4] Recently, topological nontrivial systems, including Weyl[5–8] (or Dirac)[9] and nodal-line semimetals,[10,11] have been developed swiftly, since the discovery of a topological insulator (TI) with strong spin–orbit coupling (λ).[12] Very recently, the interplay of the electronic-correlation effect and topological nontrivial states has started to attract attention[1,11,13,14] and leads to the correlated topological phases (CTPs),[1] exemplified by correlated Weyl semimetals (WSMs), axion insulators, and topological Mott insulators. WSMs that host emergent Weyl fermions in the bulk and surface Fermi arc states[5–8] are of great interest for physicists and material scientists. They have numerous intriguing properties such as the nonlinear Hall effect,[15] phonon–electron fluid behavior,[16] anomalous Hall effect (AHE),[17] anomalous Nernst effect,[18] and chiral anomaly-induced magnetotransport.[19–21] However, experimental realization of the electronic correlation effect in WSMs, that is, correlated WSMs, has been quite limited because of the rare examples[7,14] in nature.

Pyrochlore iridates ($R_2Ir_2O_7$), as a family of 5d transition metal oxides with large λ and intermediate U, are considered to be fertile ground to potentially produce the topologically nontrivial CTPs.[1,22–25] The crystal structure of $R_2Ir_2O_7$ has symmetry identical to that of the diamond lattice (**Figure 1**a and Figure S1, Supporting Information), and $R_2Ir_2O_7$ is the first real material system predicted to host Weyl fermions in solids.[5] Most $R_2Ir_2O_7$ have antiferromagnetic (AFM) ordering, known as the all-in–all-out (AIAO) state (Figure 1b). Importantly, this magnetic ordering breaks time-reversal symmetry (TRS), which leads to the magnetic WSM state with four pairs of Weyl nodes.[5] However, a charge gap usually appears at the Fermi level, since the AIAO AFM ordering can give rise to the pair annihilation of Weyl nodes. Hence, the predicted AIAO WSM state can exist only in the vicinity of the AIAO charge-gapped state, indicating an extremely narrow temperature region for the magnetic WSM state.[26] In the family of $R_2Ir_2O_7$, almost all compounds, except for R = Pr, undergo AIAO magnetic ordering below the Néel

Dr. Y. Li, T. Oh, J. Son, J. Song, Dr. M. K. Kim, Dr. D. Song, Dr. S. Kim, Prof. C. Kim, Prof. B.-J. Yang, Prof. T. W. Noh
Center for Correlated Electron Systems
Institute for Basic Science (IBS)
Seoul 08826, Republic of Korea
E-mail: yangyangli@snu.ac.kr; twnoh@snu.ac.kr
Dr. Y. Li, T. Oh, J. Son, J. Song, Dr. M. K. Kim, Dr. D. Song, Dr. S. Kim, Prof. C. Kim, Prof. B.-J. Yang, Prof. T. W. Noh
Department of Physics and Astronomy
Seoul National University
Seoul 08826, Republic of Korea
T. Oh, Prof. B.-J. Yang
Center for Theoretical Physics (CTP)
Seoul National University
Seoul 08826, Republic of Korea
Prof. S. H. Chang
Department of Physics
Chung-Ang University
Seoul 156–756, Republic of Korea

Figure 1. Phase diagram for $R_2Ir_2O_7$. a) Schematic view of the pyrochlore lattice structure. b) Schematic configuration of the AIAO AFM ordering state for A domain (left) and B domain (right). c) Phase diagram for the family of $R_2Ir_2O_7$, which is modified based on the diagrams in previous reports.[1,27] d) Exotic phase diagram of PIO in terms of a biaxial compressive strain and U. δ is the change ratio of the hopping parameter by a strain, while t_{oxy} is the hopping through oxygen. U and δ are normalized by t_{oxy}. The red line ($\delta = 0$) presents the LSM state in PIO. e) Schematic of the band renormalization due to the correlation effect (long-range Coulomb interaction), resulting in the correlated magnetic WSM state.

temperature, T_N, accompanying a metal–insulator transition (Figure 1c).[5] In contrast to the vast amount of theoretical calculations,[1,22–25] experimental observation of magnetic WSM states in $R_2Ir_2O_7$ has been extremely difficult and still remains elusive.

Bulk $Pr_2Ir_2O_7$ (PIO) is a unique metal located near the critical point of the metal–insulator transition and paramagnetic-antiferromagnetic transition of the $R_2Ir_2O_7$ family.[27] The Ir-5d electrons remain paramagnetic and metallic down to the lowest temperatures, without a major resistivity increase in PIO bulk.[28] Importantly, the Ir-5d electrons form a Luttinger semimetal (LSM) state with quadratic band touching at the Γ point[29] right across the Fermi level, which could evolve into abundant topologically nontrivial quantum phases through symmetry-breaking perturbations.[29,30] In this work, we successfully fabricated high-quality PIO strained films, and used epitaxial strain as a tuning parameter to induce the predicted magnetic WSM phase. The observed AHE demonstrates the underlying Berry curvature generated by the Weyl nodes. Magnetotransport measurements provide strong evidence for chiral anomaly of the magnetic Weyl fermions. Importantly, the temperature dependence of the planar Hall effect (PHE) coefficient can be well explained by considering the electronic correlation in the WSM state. Based on the electronic transport measurements and theoretical calculations, we report a correlated magnetic WSM state with long-range Coulomb interactions in the PIO strained film.

2. Experimental Results

2.1. Topological Phase Diagram and Epitaxial Growth of PIO

We performed mean-field calculations for the PIO system under biaxial strain, based on the Hubbard model.[31–33] The resulting phase diagram is presented in Figure 1d, in terms of U and δ (the change ratio of the hopping parameter). Note that we use δ to simulate the strain effect for the calculation,[34] and $\delta > 0$ corresponds to the compressive strain. More details about δ are provided in Figure S2, Supporting Information. Interestingly, three exotic topological phases, that is, magnetic WSM, axion insulator, and TI can be generated from the LSM system by (compressive) strain effect. Surprisingly, the "bulk-absent" AIAO AFM ordering can be developed in PIO with a small strain ($\delta < 0.3\%$ for $U = 1.39$), which leads to the previously expected magnetic WSM phase with four pairs of Weyl nodes. (Note that the term "bulk-absent" means AIAO ordering is absent in the unstrained PIO bulk or single crystal, while it

is present in our strained PIO film.) With intermediate strain ($0.3\% < \delta < 0.7\%$), the Weyl nodes are annihilated at Γ point, and a band gap appears. However, the AIAO magnetic order still remains in this region, giving rise to an axion insulator phase with a Fu-Kane Z_4 index value of 2. With further increase in strain ($\delta > 0.7\%$), the magnetic order vanishes, and the system turns out to be a paramagnetic TI.[23] More details about the calculation are provided in Figures S3 and S4, Supporting Information. This work focuses on the magnetic WSM state induced in the small strain region ($\delta < 0.3\%$). Considering the electronic correlation between Ir-5d electrons, the linear band dispersion in this magnetic WSM state can be renormalized, resulting in a correlated magnetic WSM state (Figure 1e). More details are provided below.

To explore the predicted correlated WSM phase, we fabricated high-quality PIO epitaxial film with small compressive strain using the modified solid-phase epitaxy (SPE) method. More details on the growth[35] are provided in the Experimental section and Figures S5–S7, Supporting Information. **Figure 2**a shows the X-ray diffraction pattern of the (111)-oriented PIO film on (111) yttria-stabilized zirconia (YSZ), with the bare YSZ substrate as a reference. Strong "odd-pair peaks" demonstrate the excellent crystallization of the pyrochlore phase, as the superstructure of the fluorite structure. The enlarged figure in Figure 2b shows that the PIO film is strained with the (222) peak shifted off the bulk value. Further analysis of the reciprocal space map (Figure 2c) shows that compressive strain is introduced in the (111)-plane of the PIO film, with a value of ≈0.2%. Simultaneously, the lattice is elongated along the [111] direction, consistent with the shift of the (222) peak in Figure 2b. The presence of the small strain in PIO film is crucial and responsible for the magnetic WSM state with cubic symmetry breaking and the development of AIAO ordering, consistent with the mean-field calculations (Figure 1d).

2.2. AHE in Strained PIO Film

Figure 3a presents the longitudinal resistivity, ρ_{xx}, of the PIO film as a function of temperature, measured with a Hall-bar geometry (inset of Figure 3a) without an external magnetic field. Obviously, with decreasing temperature, the PIO film and bulk single crystal samples show similar metallic behavior before a minimum value reached, and then show a small upturn in resistivity with further cooling. The minimum of resistivity in PIO film is enhanced to a slightly higher temperature (≈50 K) than that (≈40 K) for the bulk sample. The resistivity of the film is about ≈3–10 times larger than that of the bulk sample below 300 K, which could be attributed to the compressive strain in the film. With compressive strain, trigonal compression of the octahedra will be enhanced, which decreases the Ir–O orbital overlap and thus suppresses the hopping of Ir-5d electrons.[1] This also explains the resistivity of $Nd_2Ir_2O_7$ (NIO) strained film becomes significantly enhanced compared to the bulk.[34] To further check the strain effect, sample with larger compressive strain was fabricated and it shows that larger strain leads to higher resistivity (Figure S6, Supporting Information), which is consistent with our above statement. However, the influence of the crystalline order or detects on the resistivity cannot be excluded completely. The film with larger compressive strain shows higher resistivity and a new insulating behavior, which is consistent with tendence of our theoretical calculation (Figure 1d). More investigation and efforts will be done on this sample to confirm that it is the predicted axion insulator or the topological insulator in the future.

Interestingly, as shown in Figure 3b, AHE is observed in the strained PIO film with magnetic field applied along the [111] direction. For the bulk samples, a similar AHE signal was reported up to ≈1.5 K,[36–38] but the AHE signal in the film persists up to 30 K. Above 30 K, the Hall signal becomes linear, indicating that the ordinary Hall effect is dominant at elevated temperatures. Importantly, the Hall resistivity of the film sample measured at 2 K shows a hysteretic feature with a finite value at zero field. This is known as the spontaneous Hall effect (SHE), which was also reported in the bulk sample, but at lower temperature (Figure 3c). The SHE observed in the PIO film indicates both cubic symmetry breaking and TRS breaking.[34] The cubic symmetry is broken by the compressive strain at the (111) plane, and the strain-induced AIAO ordering breaks the TRS. It should be mentioned that the observed AHE in the PIO
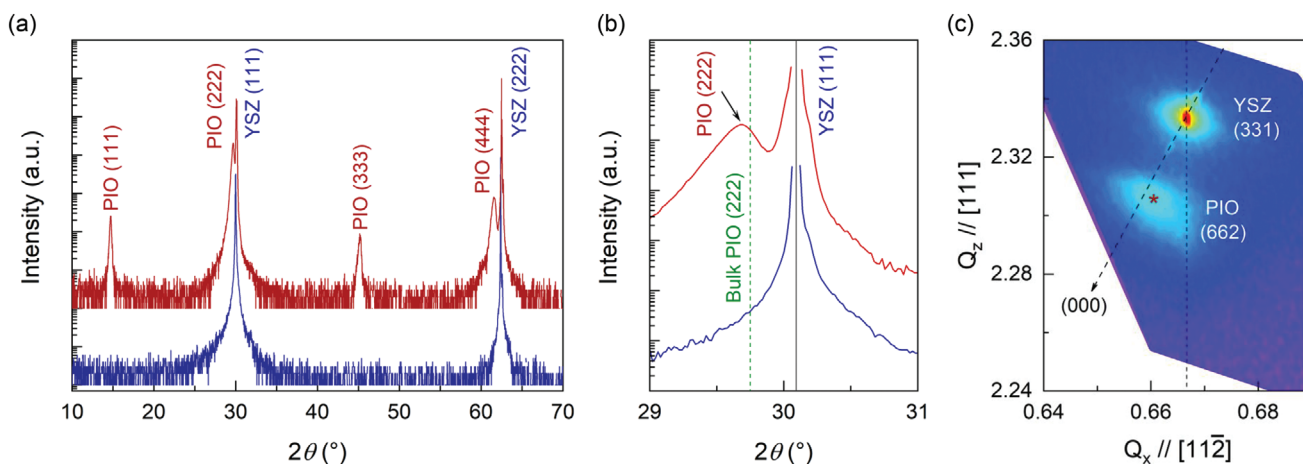
Figure 2. Structural characterization of the PIO film. a) High-resolution XRD patterns of the 40-nm-thick PIO film on the YSZ substrate and a bare YSZ substrate. b) Enlarged XRD patterns that are shown in (a). The green dashed line presents the position of the bulk PIO (222) XRD peak. c) Reciprocal space map of the PIO film in the vicinity of the YSZ (331) reflection. The * marks the peak position of the film.
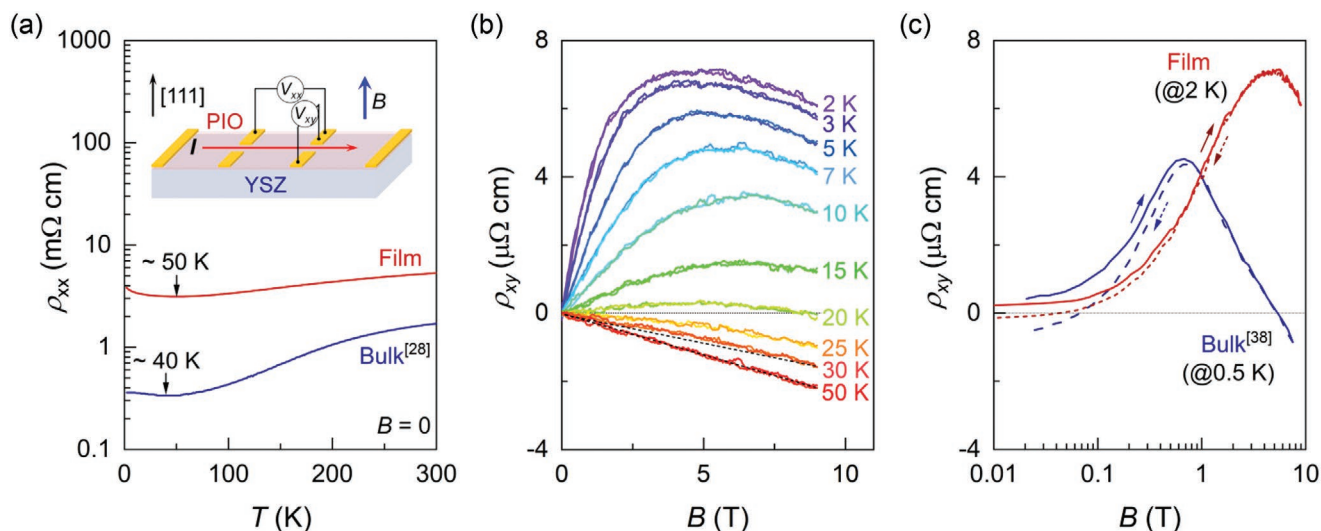
Figure 3. Resistivity and AHE in the PIO film. a) Resistivity for the PIO film and bulk single crystal.[28] The inset shows the schematic illustration of the Hall bar geometry. b) Temperature-dependent AHE collected from the PIO film. The dashed lines are eye guidelines for the linearity. c) Comparison of AHE between PIO film (2 K) and bulk[38] (0.5 K). The arrows present the field-sweeping direction.

film is different from the conventional AHE in ferromagnetic materials where the anomalous Hall resistivity is proportional to its magnetization (M).[39] In ferromagnetic materials, its Hall resistivity is $\rho_{xy} = R_0 B + 4\pi R_s M$, where the first term is the ordinary Hall effect and the second term is the AHE. The AHE in the ferromagnetic materials originates from its magnetization and spin-orbit coupling.[39] As for our PIO film with strain-induced AIAO AFM ordering, its AHE could be attributed to the non-zero Berry curvature ($\Omega_{i,k}$) induced by the nontrivial contribution of the Weyl nodes: $\sigma_{xy}^{AHE} = \sum_{i,k} n_{i,k} \Omega_{i,k}^z$, where the index i runs over the Weyl nodes and n_i is the occupation number in node i.[40]

2.3. Magnetotransport Properties in Strained PIO Film

To obtain further insight into the magnetic Weyl fermions, we performed magnetotransport measurements on the PIO film by applying the magnetic field **B** perpendicular and parallel to the current **I** direction. It has been reported that the bulk PIO sample has a huge positive transverse magnetoresistivity (TMR: **B** ∏ **I**) when magnetic field is applied along the [111] direction (Figure S8a, Supporting Information). The positive TMR in bulk PIO[38] can be understood by the localization of electrons due to the Lorentz force, which is common when magnetic field is applied to nonmagnetic/paramagnetic metallic systems. Surprisingly, a negative TMR with an upturn at high field is observed at 2 K in the film sample (**Figure 4**a and Figure S8a, Supporting Information). The negative TMR in the strained PIO film unambiguously indicates a distinct state from the bulk PIO that is a paramagnetic LSM. Notably, the upturn in negative TMR in the PIO film is quite similar to that of the NIO single crystals under pressure.[26] It is well known that NIO has intrinsic AIAO magnetic ordering at ≈30 K in bulk.[26,27] The conversion from negative to positive (upturn) in the TMR can be interpreted by the switching from a 4-in–0-out (4/0) state to a

3-in–1-out (3/1) state in the AIAO ordered phase, as mentioned for the NIO bulk.[26] According to the previous calculation,[32] the band structure of the pyrochlore iridates is very sensitive to their magnetic ordering. When the magnetic field is applied along [111], the magnetic ordering of pyrochlore iridates switches from 4/0 to 3/1 state, and the band structure near the Fermi level changes drastically when the magnetic ordering switches. For instance, according to the theoretical calculations, the Weyl semimetal phase in 4/0 state has four pairs of Weyl points, which turns into another Weyl semimetal with three pairs of Weyl points in 3/1 state. Such a change of low energy band structure can significantly affect the low energy density of states and the transport properties. Therefore, the density of states at the Fermi level can be decreased in the 3/1 state as it is indicated in the $Nd_2Ir_2O_7$ case,[26] resulting in the upturn from negative to positive in the TMR. Besides, it should be point out that the thickness of our film is about ≈40 nm, which is beyond the quantum confinement region and can be regarded as a 3D system. With the strain-induced AIAO ordering, we believe it is reasonable to compare the PIO film with the NIO bulk. The PIO film also shows similar hysteretic behavior (Figure 4a), which disappears at 15 K (Figure 4b and Figure S8b, Supporting Information). Above 15 K, the TMR become positive and linear.

Specifically, in the hysteretic loop seen in the TMR data (Figure 4a), the ρ_{xx} for the field-decreasing process (blue lines) is larger than that for the field-increasing process (red lines) in the positive field region, with the opposite being true in the negative field region. This hysteresis feature is the same as that observed in the NIO single crystals,[26] and can be explained by the unique configurations of the AIAO ordering in $R_2Ir_2O_7$. As shown in Figure 1b, there are two degenerate magnetic domains in the AIAO AFM state, that is, the all-in–all-out/AIAO A domain and the all-out–all-in/AOAI B domain, which are connected by the time-reversal operation.[41] Each of these two domains can be aligned by the external magnetic field, applied along the [111] or in the opposite direction.[26,41] The hysteresis loop at 5 K is shown in detail in Figure 4c. The butterfly-like
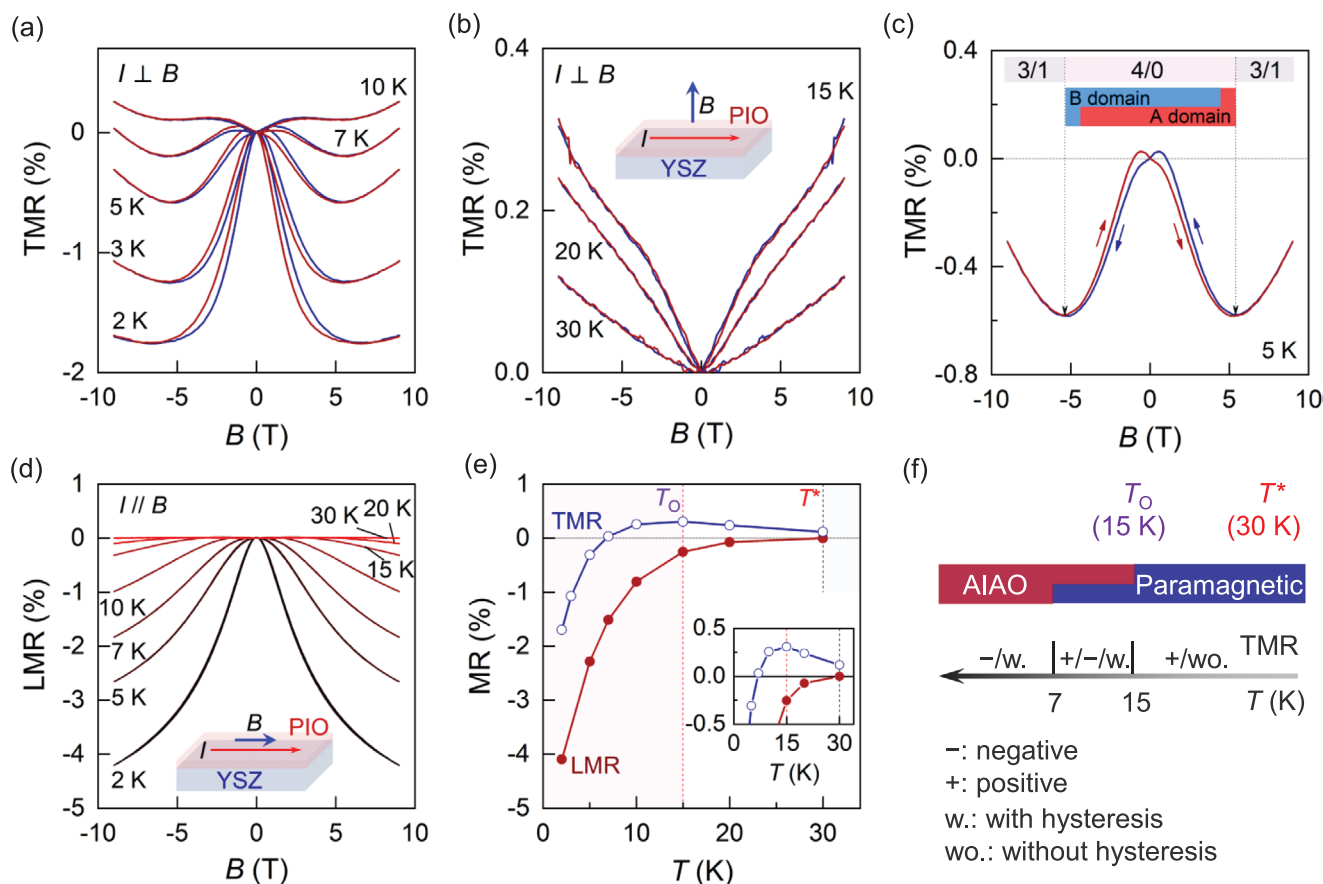
Figure 4. Magnetotransport property of the PIO film. a,b) TMR in the PIO film measured at different temperatures: a) $T < T_O$ and b) $T_O \leq T \leq T^*$, respectively. The blue and red lines are on field-decreasing process and field-increasing process, respectively. Inset in (b) shows the experimental configuration of TMR. c) Magnified TMR result measured at 5 K in (a). d) Temperature dependence of the LMR. Inset shows the experimental configuration of LMR. e) Temperature dependence of the TMR and LMR values at 9 T. f) Phase transition of the PIO film with temperature. −, +, w., and wo., are denoted as negative component, positive component, with hysteresis, and without hysteresis for TMR.

hysteresis within ±4.5 T indicates the multi-domain states. Above ±4.5 T, they can be aligned to a single domain state. Further increasing the field will switch the spins, so the system is transformed into the 3/1 state. The hysteresis behavior observed in the TMR results indicates that AIAO ordering does indeed develop in the strained PIO film (below 15 K), which is in good agreement with our calculations (Figure 1d). Note that the local Ir moments has been detected in the previous film sample,[42] consistent with our results. Since our PIO film is about ≈40 nm, which is far from the requirements for the Neutron scattering measurements.[43] Thus, we cannot use neutron scattering to confirm the AIAO AFM ordering in our PIO strained film. More advanced techniques will be pursued in the future.

According to the mean-field calculation, the quadratic band touching in LSM is very sensitive to the AIAO ordering, and it could be in the magnetic WSM state with TRS breaking. Hence, we further measured the longitudinal magnetoresistivity (LMR: **B || I**) to detect the chiral anomaly associated with the Weyl fermions. As expected, negative LMR without hysteresis is observed below 30 K (Figure 4d), which is considered as a signature of the chiral anomaly of WSMs originating from the charge pumping effect between the Weyl nodes (Figure S8c, Supporting Information).[19,21,44] At low field region, the LMR

has a small positive component (Figure S8d, Supporting Information), which is due to the weak antilocalization in the topological materials.[19,21] Figure 4e summarizes the TMR and LMR values at 9 T. Below 30 K (denoted by T^*), the LMR (@ 9 T) is always negative, while the TMR (@ 9 T) is positive and turns to negative at 5 K with a peak around 15 K. This intriguing TMR behavior might be understood in terms of the competition between the Lorentz force (positive component) and AIAO ordering (negative component).

In the range of 15–30 K, the TMR (@ 9 T) is positive and increases with cooling indicating a paramagnetic phase wherein the Lorentz force contribution is dominant. Below 15 K (denoted by T_O), AIAO ordering appears, so the TMR (@ 9 T) starts to decrease with cooling. Below 7 K, clear hysteresis is observed in the field-dependent TMR (Figure 4a) and the TMR value at 9 T (Figure 4e) becomes negative, demonstrating that the contribution of the AIAO magnetic ordering is dominant below 7 K. As a consequence, coexistence of the paramagnetic and AIAO phase is seen in the range of 7–15 K. The coexistence is implied in Figure S8b (Supporting Information), where the TMR at 10 K shows a positive component ($0 < B < ≈3.0$ T, and $≈5.6$ T $< B$), a negative component ($≈3.0$ T $< B < ≈5.6$ T), and hysteresis behavior. To show

**ADVANCED
SCIENCE NEWS**

www.advancedsciencenews.com

**ADVANCED
MATERIALS**

www.advmat.de

the magnetic phase transitions with temperature for the PIO film more clearly, a schematic phase transition is presented in Figure 4f, based on the TMR results. It should be mentioned that we did not observe the quantum oscillations in our PIO film. That is because the mobility in the PIO system is very low (single crystal:[36] ≈10 cm^2 V^{-1} s^{-1}; our film: ≈ 0.74 cm^2 V^{-1} s^{-1}), which is far from those observed in TaAs[19] or SrRuO$_3$[45] systems and the requirement for the quantum oscillation at few Tesla (>10^3 cm^2 V^{-1} s^{-1}).[46,47] Moreover, the PIO is known as a heavy fermion system with strong hybridization between the Pr 4f and Ir 5d electrons.[28] Its effective mass is also large so that the oscillation conditions cannot be fulfilled.[47] Hence, we cannot observe the quantum oscillation in our film at few Tesla. Further improvements of the film quality would be needed for further quantum transport measurements in the future.

2.4. PHE in Strained PIO Film

Since the current jetting effect could also cause negative LMR,[48] then negative LMR alone cannot confirm the chiral anomaly. With this concern, we also performed PHE measurements (**Figure 5**a) on the PIO film to exclude the current jetting and

confirm the existence of the chiral anomaly[21,49–53] and AIAO ordering. The planar Hall conductivity, σ_{xy}^{PHE}, for the PIO film in the magnetic WSM state can be written as

$$\sigma_{xy}^{PHE} = \sigma_{xy}^{Chiral} + \sigma_{xy}^{AIAO} \tag{1}$$

where σ_{xy}^{Chiral} and σ_{xy}^{AIAO} are the contributions from the chiral anomaly and AIAO ordering, respectively. It is well known that the σ_{xy}^{Chiral} can be written as

$$\sigma_{xy}^{Chiral}(\phi) = \Delta\sigma_{chiral}\sin\phi\cos\phi \tag{2}$$

where $\Delta\sigma_{chiral} = \sigma_{\parallel} - \sigma_{\perp}$ originates from the chiral anomaly.[20] $\sigma_{\perp}$ and $\sigma_{\parallel}$ are the conductivity when the magnetic field is perpendicular and parallel to the current, respectively. φ is the angle between the magnetic field and the current.

As shown in Figure 5b, we cannot explain the observed PHE result based only on the typical chiral anomaly, which has a simple sin 2φ dependence in Equation (2) (blue dashed line in Figure 5b). As demonstrated earlier in the magnetotransport results, the strained PIO film can have AIAO ordering. Then, in the pyrochlore lattice, a higher-rank magnetic multipole, called the A$_2$-octupole (ω_{xyz})[34,54] can be formed by the clusters
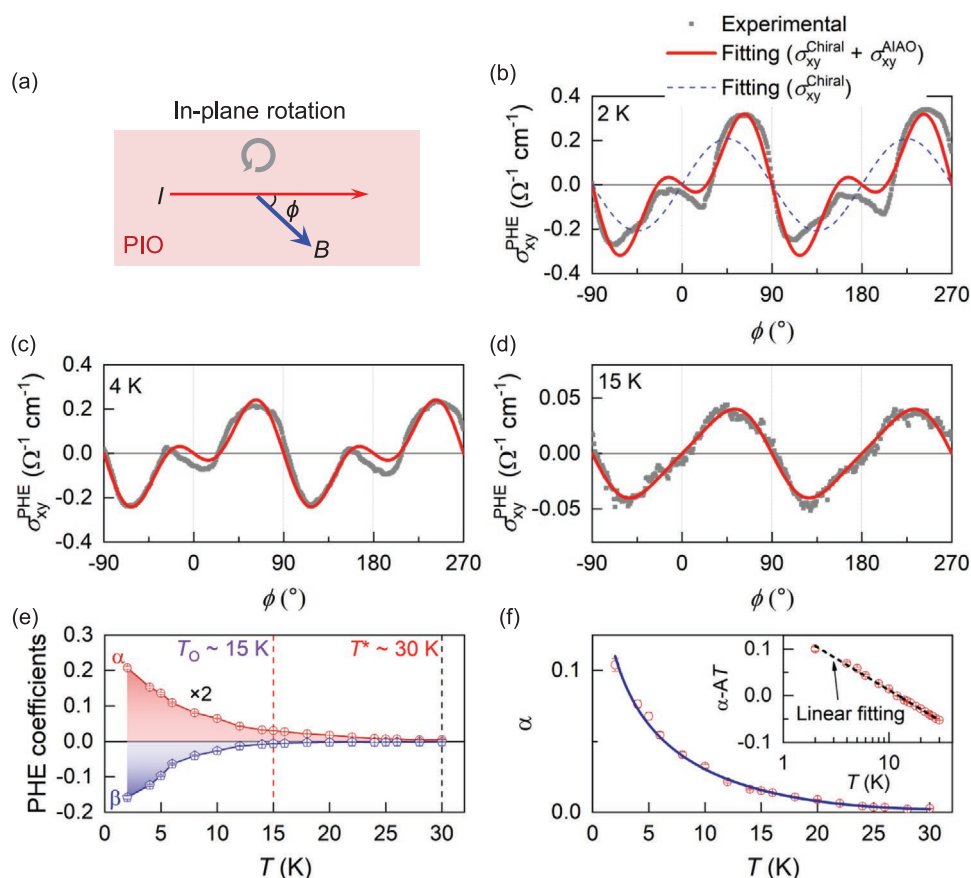
Figure 5. PHE in the PIO film. a) Schematic of the experimental configuration for PHE measurement. b–d) Angle (ϕ)-dependence of the σ_{xy}^{PHE}, measured at 2, 4, and 15 K with external magnetic field ± 9 T, respectively. Equations (2) and (4) are used for the fitting. e) Temperature dependence of the PHE coefficients α and β in Equation (4), which originates from the chiral anomaly and AIAO magnetic ordering, respectively. f) Renormalization group analysis for the chiral anomaly (α) term due to the correlation effect. Renormalized fitting function (blue solid line): $f(x) = AT + B\ln T + C$. A, B, and C are constants. The inset shows the strong ln$T$ component in α.

of spins. Even though AIAO ordering does not carry any dipole moments, an A_2-octupole can induce the orthogonal magnetization $M_\perp$ when the magnetic field is applied.[54] Note that the direction of the orthogonal magnetization is perpendicular to the field.

Thus, in addition to the chiral anomaly, the orthogonal magnetization can make an additional contribution to the PHE. Considering the contribution from the orthogonal magnetization, the σ_{xy}^{PHE} in the PIO film can be written as

$$\sigma_{xy}^{\text{PHE}}(\phi) = \sigma_3 H^2 \sin\phi\cos\phi + \sigma_4 \frac{\omega_{xyz}^2}{12} H^4 \sin 4\phi \qquad (3)$$

where σ_3 and σ_4 are constants, H is the magnetic field, and ω_{xyz} is the A_2-octupole moment. The first term is derived from the chiral anomaly, while the second originates from the AIAO ordering. By setting two parameters $\alpha = \frac{\sigma_3 H^2}{2}$ and $\beta = \frac{\sigma_4 \omega_{xyz}^2}{12} H^4$, we get

$$\sigma_{xy}^{\text{PHE}}(\phi) = \sigma_{xy}^{\text{Chiral}} + \sigma_{xy}^{\text{AIAO}} = \alpha \sin 2\phi + \beta \sin 4\phi \qquad (4)$$

where we denote α and β as the chiral anomaly and A_2-octupole induced PHE coefficients, respectively.

The experimental σ_{xy}^{PHE} and fitting results are shown in Figure 5b–d (for more details, see Figures S9–S11, Supporting Information). Clearly, below $T_O \approx 15$ K, fitting with the chiral anomaly and AIAO ordering (Equation (4)) is excellent, and much better than that only with the chiral anomaly (Equation (2)) (Figure 5b and Figure S11, Supporting Information), demonstrating that the AIAO ordering has been developed in the PIO film. The variation between the fitting (Equation (4)) and experimental data (Figure 5b–d) could result from the spin fluctuation. In the range of 15 K (T_O) < T < 30 K (T^*), the magnetic ordering vanishes as β approaches 0 (Figure 5e), indicating that AIAO ordering is developed below 15 K, consistent with the TMR data (Figure 4f). The chiral anomaly exists with a finite α value up to 30 K (Figure 5e), demonstrating a WSM state is generated by the external magnetic field[55] from the paramagnetic state (Figure 4f) in the range of 15 K (T_O) < T < 30 K (T^*). To check the reproducibility of our film and experimental measurements, another reference sample has been made. As expected, consistent results (for more details, see Figures S12–S15, Supporting Information) has been obtained from the new fabricated PIO film. Same conclusion can be made as the one we described above. Besides, with the combination of negative LMR and PHE results, we can confirm the chiral anomaly with AIAO ordering and exclude the current jetting effect in our film.

The temperature dependence of the PHE coefficient α can only be understood by including the electronic correlation in a WSM state.[56] Through a dimensional analysis, σ_3 can be written as

$$\sigma_3 \propto \frac{e^2}{\hbar} \frac{v_F^3 e^2}{\mu^2} \tau \qquad (5)$$

where $\hbar$ is the Planck constant, e is the electron charge, v_F is the Fermi velocity, τ is the relaxation time, and μ is the chemical

potential. This result is consistent with previous report.[21] To shed light on the temperature dependence of σ_3 (or α), we need to study the temperature dependence of Fermi velocity v_F, relaxation time τ, and chemical potential μ. The temperature dependence can be obtained from a one-loop calculation in a WSM with long-range Coulomb interactions.[56]

$$v_F(T) = v_{F0}\left(1 + \frac{N+2}{3\pi}\alpha_0 \ln\frac{\hbar\Lambda}{k_B T}\right)^{\frac{2}{N+2}} \qquad (6)$$

and $\mu \propto \left(1 + \frac{\alpha_0}{\pi\mu_0} T \ln\frac{\hbar\Lambda}{k_B T}\right) \qquad (7)$

where N is the number of Weyl nodes, $\alpha_0 = \frac{e^2}{\varepsilon v_F}$ is the bare dimensionless coupling constant, and Λ is the cutoff momentum. The transport relaxation time of a WSM with long-range Coulomb interactions at low temperature can be written as[57]

$$\tau \propto 1 + \frac{2\pi^2}{3}\left(\frac{T}{T_F}\right)^2 \qquad (8)$$

where T_F is the Fermi temperature. Hence, for small coupling and low temperature, the temperature dependence of $\alpha = \frac{\sigma_3 H^2}{2}$ in the correlated WSM state can be approximated to

$$\alpha \propto A T + B \ln T + C \qquad (9)$$

where A–C are constants, and the $\ln T$ and T terms arise from the renormalization of the Fermi velocity and chemical potential, respectively (for more details of the analysis of PHE, see Supporting Information.) As shown in Figure 5f, the experimental data are in excellent agreement with the renormalization group calculation, demonstrating the renormalization effect of the electronic correlation in the WSM state. A strong $\ln T$ component is obtained in α (see inset of Figure 5f), which indicates the enhancement of Fermi velocity with long-range Coulomb interactions.[58] A similar renormalization effect due to the long-range Coulomb interaction has only been reported in graphene,[11,58,59] which is a 2D Dirac system. Our results indicate the emergence of a correlated WSM state renormalized logarithmically (see Figure 1e) due to long-range Coulomb interactions. Note that this correlated WSM state requires both the AIAO ordering and semimetal state for pyrochlore iridates. Unfortunately, no known pyrochlore iridate material can hold both conditions intrinsically. Thus, strain is the crucial parameter to induce the correlated WSM state in PIO.

3. Conclusion

A novel correlated magnetic WSM state can be achieved in the strained PIO film, consistent with the theoretical calculations. Moreover, the temperature dependence of the chiral anomaly induced PHE coefficient, α, can be attributed to the electronic correlation in WSMs that renormalizes the Fermi velocity and chemical potential. Strain-induced "bulk-absent" magnetic

ordering in PIO film lead to the correlated WSM state, which provides a route for strain-engineering of the CTPs in $R_2Ir_2O_7$. According to the mean-field calculation, an axion insulator and strong TI can be produced by larger strain in PIO, which demonstrates that the PIO system is a promising platform for exploring CTPs. Furthermore, this work highlights the interplay of strain, topology, and magnetism in correlated systems, which would promote future investigations on correlated topological nontrivial states in other quantum systems.

4. Experimental Section

Self-Consistent Mean-Field Calculations: The Hubbard model for the strained PIO thin film was performed, acquiring the ground state and electronic structures by the self-consistent mean-field method. $24 \times 24 \times 24$ and $32 \times 32 \times 32$ k-point mesh was adopted and it was confirmed that the results were consistent. More details can be found in Supporting Information.

Theoretical Estimation of PHE: A general form of σ_{xy}^{PHE} was found by considering the Onsager's reciprocal relation and cubic symmetry. Since the system was antiferromagnetic and carrying a higher-rank magnetic multipole, the specific form of σ_{xy}^{PHE} was estimated with an orthogonal magnetization, which arises when the higher-rank multipole couples to the magnetic field. Through dimensional analysis, the coefficients of the chiral anomaly and orthogonal magnetization-induced PHE were predicted. The temperature dependence of the chiral anomaly-induced PHE coefficient α was obtained through a one-loop calculation in a WSM with the electronic correlation effect. More details are provided in Supporting Information.

Sample Fabrication and Characterization: The PIO (111) epitaxial films were fabricated on commercial YSZ (111) single crystal substrates via a modified solid phase epitaxy (SPE) method. Initially, an amorphous PIO film was deposited at 600 °C by pulsed laser deposition using a 248 nm KrF laser, while the amorphous layer was deposited at room temperature using the conventional SPE method. The laser fluence and repetition rate were fixed to ≈1.5 J cm^{-2} and 5 Hz, respectively. The oxygen pressure of the chamber was set to 50 mTorr. After deposition, the PIO films were crystallized by post-annealing in a partially sealed tube with IrO_2 powder aside. The post-annealing process was performed in a box furnace in air at 1000 °C for 1 h. The PIO and IrO_2 targets, used for the film growth, were prepared by the conventional hot-press method. More details of the sample growth are shown in Supporting Information. After the crystallization, all films were characterized by a D8 Discover high-resolution diffractometer (Bruker), operated at 40 kV and 60 mA.

Transport Measurements: The transport properties of the PIO (111) epitaxial films were measured using the standard four-probe method in a commercial Quantum Design physical property measurement system (PPMS) equipped with a 9 T superconducting magnet. A Ti/Au (10/60 nm) bilayer was deposited as electrodes by thermal evaporation, with the Hall bar geometry (Inset of Figure 3a). Al wires were used to connect the samples and PPMS pucks. Special attention was paid to align the sample on the PPMS puck that has the rotation option. During the measurements, 10 μA current was applied along the [$1\bar{1}0$] direction. The planar Hall resistivity and conductivity were obtained by

$$\rho_{xy}^{PHE} = \frac{\rho_{xy}^{PHE}(B) + \rho_{xy}^{PHE}(-B)}{2} \quad \text{and} \quad \sigma_{xy}^{PHE} = -\frac{\rho_{xy}^{PHE}}{\rho_{xx}^2 + (\rho_{xy}^{PHE})^2}, \quad \text{respectively.}$$

More experimental results and details are shown in Supporting Information.

Supporting Information

Supporting Information is available from the Wiley Online Library or from the author.

Conflict of Interest

The authors declare no conflict of interest.

Data Availability Statement

Research data are not shared.

[1] W. Witczak-Krempa, G. Chen, Y. B. Kim, L. Balents, *Annu. Rev. Condens. Matter Phys.* **2014**, *5*, 57.

[2] S. Y. Kim, M.-C. Lee, G. Han, M. Kratochvilova, S. Yun, S. J. Moon, C. Sohn, J.-G. Park, C. Kim, T. W. Noh, *Adv. Mater.* **2018**, *30*, 1704777.

[3] E. Dagotto, T. Hotta, A. Moreo, *Phys. Rep.* **2001**, *344*, 1.

[4] P. A. Lee, N. Nagaosa, X.-G. Wen, *Rev. Mod. Phys.* **2006**, *78*, 17.

[5] X. Wan, A. M. Turner, A. Vishwanath, S. Y. Savrasov, *Phys. Rev. B* **2011**, *83*, 205101.

[6] H. Weng, C. Fang, Z. Fang, B. A. Bernevig, X. Dai, *Phys. Rev. X.* **2015**, *5*, 011029.

[7] K. Kuroda, T. Tomita, M.-T. Suzuki, C. Bareille, A. A. Nugroho, P. Goswami, M. Ochi, M. Ikhlas, M. Nakayama, S. Akebi, R. Noguchi, R. Ishii, N. Inami, K. Ono, H. Kumigashira, A. Varykhalov, T. Muro, T. Koretsune, R. Arita, S. Shin, T. Kondo, S. Nakatsuji, *Nat. Mater.* **2017**, *16*, 1090.

[8] S. Y. Xu, I. Belopolski, N. Alidoust, M. Neupane, G. Bian, C. Zhang, R. Sankar, G. Chang, Z. Yuan, C.-C. Lee, S.-M. Huang, H. Zheng, J. Ma, D. S. Sanchez, B. K. Wang, A. Bansil, F. Chou, P. P. Shibayev, H. Lin, S. Jia, M. Z. Hasan, *Science* **2015**, *349*, 613.

[9] J. Xiong, S. K. Kushwaha, T. Liang, J. W. Krizan, M. Hirschberger, W. Wang, R. J. Cava, N. P. Ong, *Science* **2015**, *350*, 413.

[10] J. Ahn, D. Kim, Y. Kim, B. J. Yang, *Phys. Rev. Lett.* **2018**, *121*, 106403.

[11] Y. Shao, A. N. Rudenko, J. Hu, Z. Sun, Y. Zhu, S. Moon, A. J. Millis, S. Yuan, A. I. Lichtenstein, D. Smirnov, Z. Q. Mao, M. I. Katsnelson, D. N. Basov, *Nat. Phys.* **2020**, *16*, 636.

[12] J. E. Moore, *Nature* **2010**, *464*, 194.

[13] D. Pesin, L. Balents, *Nat. Phys.* **2010**, *6*, 376.

[14] Y. Xu, J. Zhao, C. Yi, Q. Wang, Q. Yin, Y. Wang, X. Hu, L. Wang, E. Liu, G. Xu, L. Lu, A. A. Soluyanov, H. Lei, Y. Shi, J. Luo, Z.-G. Chen, *Nat. Commun.* **2020**, *11*, 3985.

[15] Q. Ma, S.-Y. Xu, H. Shen, D. MacNeill, V. Fatemi, T.-R. Chang, A. M. Mier Valdivia, S. Wu, Z. Du, C.-H. Hsu, S. Fang, Q. D. Gibson,

K. Watanabe, T. Taniguchi, R. J. Cava, E. Kaxiras, H.-Z. Lu, H. Lin, L. Fu, N. Gedik, P. Jarillo-Herrero, *Nature* **2019**, *565*, 337.

[16] G. B. Osterhoudt, Y. Wang, C. A. C. Garcia, V. M. Plisson, J. Gooth, C. Felser, P. Narang, K. S. Burch, *Phys. Rev. X* **2021**, *11*, 011017.

[17] S. Nakatsuji, N. Kiyohara, T. Higo, *Nature* **2015**, *527*, 212.

[18] M. Ikhlas, T. Tomita, T. Koretsune, M.-T. Suzuki, D. N. Hamane, R. Arita, Y. Otani, S. Nakatsuji, *Nat. Phys.* **2017**, *13*, 1085.

[19] X. Huang, L. Zhao, Y. Long, P. Wang, D. Chen, Z. Yang, H. Liang, M. Xue, H. Weng, Z. Fang, X. Dai, G. Chen, *Phys. Rev. X* **2015**, *5*, 031023.

[20] S. Nandy, G. Sharma, A. Taraphder, S. Tewari, *Phys. Rev. Lett.* **2017**, *119*, 176804.

[21] D. T. Son, B. Z. Spivak, *Phys. Rev. B* **2013**, *88*, 104412.

[22] B. J. Yang, N. Nagaosa, *Phys. Rev. Lett.* **2014**, *112*, 246402.

[23] B. J. Yang, Y. Kim, *Phys. Rev. B* **2010**, *82*, 085111.

[24] E. Moon, C. Xu, Y. Kim, L. Balents, *Phys. Rev. Lett.* **2013**, *111*, 206401.

[25] P. Goswami, B. Roy, S. Sarma, *Phys. Rev. B* **2017**, *95*, 085120.

[26] K. Ueda, R. Kaneko, H. Ishizuka, J. Fujioka, N. Nagaosa, Y. Tokura, *Nat. Commun.* **2018**, *9*, 3032.

[27] K. Matsuhira, M. Wakeshima, Y. Hinatsu, S. Takagi, *J. Phys. Soc. Jpn.* **2011**, *80*, 094701.

[28] S. Nakatsuji, Y. Machida, Y. Maeno, T. Tayama, T. Sakakibara, J. van Duijn, L. Balicas, J. N. Millican, R. T. Macaluso, J. Y. Chan, *Phys. Rev. Lett.* **2006**, *96*, 087204.

[29] T. Kondo, M. Nakayama, R. Chen, J. J. Ishikawa, E.-G. Moon, T. Yamamoto, Y. Ota, W. Malaeb, H. Kanai, Y. Nakashima, Y. Ishida, R. Yoshida, H. Yamamoto, M. Matsunami, S. Kimura, N. Inami, K. Ono, H. Kumigashira, S. Nakatsuji, L. Balents, S. Shin, *Nat. Commun.* **2015**, *6*, 10042.

[30] S. Ghorashi, P. Hosur, C. Ting, *Phys. Rev. B* **2018**, *97*, 205402.

[31] J. Luttinger, *Phys. Rev.* **1956**, *102*, 1030.

[32] T. Oh, H. Ishizuka, B.-J. Yang, *Phys. Rev. B* **2018**, *98*, 144409.

[33] W. Witczak-Krempa, A. Go, Y. B. Kim, *Phys. Rev. B* **2013**, *87*, 155101.

[34] W. J. Kim, T. Oh, J. Song, E. K. Ko, Y. Li, J. Mun, B. Kim, J. Son, Z. Yang, Y. Kohama, M. Kim, B.-J. Yang, T. W. Noh, *Sci. Adv.* **2020**, *6*, eabb1539.

[35] W. J. Kim, E. K. Ko, S. Y. Kim, B. Kim, T. W. Noh, *Curr. Appl. Phys.* **2019**, *19*, 400.

[36] Y. Machida, S. Nakatsuji, Y. Maeno, T. Tayama, T. Sakakibara, S. Onoda, *Phys. Rev. Lett.* **2007**, *98*, 057203.

[37] Y. Machida, S. Nakatsuji, S. Onoda, T. Tayama, T. Sakakibara, *Nature* **2010**, *463*, 210.

[38] L. Balicas, S. Nakatsuji, Y. Machida, S. Onoda, *Phys. Rev. Lett.* **2011**, *106*, 217204.

[39] N. Nagaosa, J. Sinova, S. Onoda, A. H. MacDonald, N. P. Ong, *Rev. Mod. Phys.* **2010**, *82*, 1539.

[40] T. Liang, J. Lin, Q. Gibson, S. Kushwaha, M. Liu, W. Wang, H. Xiong, J. A. Sobota, M. Hashimoto, P. S. Kirchmann, Z.-X. Shen, R. J. Cava, N. P. Ong, *Nat. Phys.* **2018**, *14*, 451.

[41] T. C. Fujita, Y. Kozuka, M. Uchida, A. Tsukazaki, T. Arima, M. Kawasaki, *Sci. Rep.* **2015**, *5*, 9711.

[42] L. Guo, N. Campbell, Y. Choi, J.-W. Kim, P. J. Ryan, H. Huyan, L. Li, T. Nan, J.-H. Kang, C. Sundahl, X. Pan, M. S. Rzchowski, C.-B. Eom, *Phys. Rev. B* **2020**, *101*, 104405.

[43] Z.-D. Fu, P. Kögerler, U. Rücker, Y. Su, R. Mittal, T. Brückel, *New J. Phys.* **2010**, *12*, 083044.

[44] R. D. d. Reis, M. O. Ajeesh, N. Kumar, F. Arnold, C. Shekhar, M. Naumann, M. Schmidt, M. Nicklas, E. Hassinger, *New J. Phys.* **2016**, *18*, 085006.

[45] K. Takiguchi, Y. K. Wakabayashi, H. Irie, Y. Krockenberger, T. Otsuka, H. Sawada, S. A. Nikolaev, H. Das, M. Tanaka, Y. Taniyasu, H. Yamamoto, *Nat. Commun.* **2020**, *11*, 4969.

[46] T. Ando, A. B. Fowler, F. Stern, *Rev. Mod. Phys.* **1982**, *54*, 437.

[47] A. D. Caviglia, S. Gariglio, C. Cancellieri, B. Sacépé, A. Fête, N. Reyren, M. Gabay, A. F. Morpurgo, J.-M. Triscone, *Phys. Rev. Lett.* **2010**, *105*, 236802.

[48] M. Hirschberger, S. Kushwaha, Z. Wang, Q. Gibson, S. Liang, C. A. Belvin, B. A. Bernevig, R. J. Cava, N. P. Ong, *Nat. Mater.* **2016**, *15*, 1161.

[49] A. Burkov, *Phys. Rev. B* **2017**, *96*, 041110(R).

[50] P. Li, C. H. Zhang, J. W. Zhang, Y. Wen, X. X. Zhang, *Phys. Rev. B* **2018**, *98*, 121108(R).

[51] F. Seitz, *Phys. Rev.* **1950**, *79*, 372.

[52] A. A. Taskin, H. F. Legg, F. Yang, S. Sasaki, Y. Kanai, K. Matsumoto, A. Rosch, Y. Ando, *Nat. Commun.* **2017**, *8*, 1340.

[53] S. Nandy, A. Taraphder, S. Tewari, *Sci. Rep.* **2018**, *8*, 14983.

[54] T. Liang, T. H. Hsieh, J. J. Ishikawa, S. Nakatsuji, L. Fu, N. P. Ong, *Nat. Phys.* **2017**, *13*, 599.

[55] T. Ohtsuki, Z. Tian, A. Endo, M. Halim, S. Katsumoto, Y. Kohama, K. Kindo, M. Lippmaa, S. Nakatsuji, *Proc. Natl. Acad. Sci. USA* **2019**, *116*, 8803.

[56] P. Hosur, S. A. Parameswaran, A. Vishwanath, *Phys. Rev. Lett.* **2012**, *108*, 046602.

[57] S. D. Sarma, E. H. Hwang, H. Min, *Phys. Rev. B* **2015**, *91*, 035201.

[58] D. E. Sheehy, J. Schmalian, *Phys. Rev. Lett.* **2007**, *99*, 226803.

[59] V. N. Kotov, B. Uchoa, V. M. Pereira, *Rev. Mod. Phys.* **2012**, *84*, 1067.